SCIENCE CHINA
Information Sciences

• RESEARCH PAPER •

March 2026, Vol. 69, Iss. 3, 132405:1–132405:10
https://doi.org/10.1007/s11432-025-4581-8

InGaN-based high-speed mini laser diode surpasses PAM-4 visible light links by over 30 Gbps

Junhui HU[1], Zhenqian GU[1], Haolin JIA[1], Zhen YANG[1], Zengxin LI[1], Jiabin WU[1], Leihao SUN[1], Aolong SUN[1], Ouhan HUANG[1], Changsheng XIA[2], Boon S. OOI[3], Jianyang SHI[1], Ziwei LI[1], Junwen ZHANG[1], Shaohua YU[4], Nan CHI[1] & Chao SHEN[1*]

[1]*Key Laboratory for Information Science of Electromagnetic Waves (MoE), College of Future Information Technology, Fudan University, Shanghai 200438, China*
[2]*GMPT Company Ltd., Shanghai 201210, China*
[3]*Photonics Laboratory, King Abdullah University of Science and Technology (KAUST), Thuwal 23955, Saudi Arabia*
[4]*Pengcheng Laboratory, Shenzhen 518055, China*

Received 1 May 2025/Revised 28 June 2025/Accepted 4 September 2025/Published online 3 February 2026

Abstract The advancement of next-generation wireless communication technologies demands ultra-high-speed visible light communication (VLC) systems to support applications ranging from underwater optical links to terrestrial high-capacity networks. Indium gallium nitride (InGaN)-based blue laser diodes (LDs) have emerged as pivotal components for high-speed VLC due to their superior modulation bandwidth. However, achieving data rates beyond 30 Gbps under simple modulation schemes remains challenging, as the bandwidth is limited by carrier transport effects, low differential gain in multiple quantum wells (MQWs) induced by carrier accumulation, and significant damping effects. In this work, we present an InGaN-based blue mini-LD architecture featuring triple $In_{0.18}Ga_{0.82}N/In_{0.05}Ga_{0.95}N$ QWs, 50 nm waveguide layer, and a 300 μm short cavity, designed to address these bottlenecks. Experimental characterization demonstrates a record-breaking −3 dB bandwidth of 8.4 GHz with a low damping factor of 0.211 ns for InGaN blue LD, surpassing prior state-of-the-art designs. Using this device, a VLC system that employs standard on-off keying (OOK) and four-level pulse amplitude modulation (PAM4) achieves unprecedented data rates of 20 and 33 Gbps, respectively. Under the Shannon limit, the data rate can exceed 37 Gbps. Our work resolves critical limitations in large-bandwidth InGaN LD development, providing a scalable pathway to meet the increasing demands of high-speed VLC networks, underwater communications, optical interconnects, and other bandwidth-intensive optical wireless applications.

Keywords visible light communication, InGaN laser diode, mini-cavity, bandwidth, damping effect, data rate

Citation Hu J H, Gu Z Q, Jia H L, et al. InGaN-based high-speed mini laser diode surpasses PAM-4 visible light links by over 30 Gbps. Sci China Inf Sci, 2026, 69(3): 132405, https://doi.org/10.1007/s11432-025-4581-8

1 Introduction

Next-generation wireless communication technology aims to extend the coverage of 5th generation mobile communication technology (5G) beyond terrestrial networks to underwater, aerial, and satellite environments [1]. This requires beyond 5G/6G communication technologies to deeply integrate various wireless communication methods to build a high-speed, all-encompassing, and broad coverage network system [2–5]. Visible light communication (VLC) is an emerging optical communication technology to meet these demands [6–8], which can support high-speed data link [9–11], unlicensed and rich spectrum resources [12, 13], high-security [14], and electromagnetic interference-free [15]. Especially, due to the low loss window of 450–570 nm in underwater environments [16], VLC can enable high-speed underwater optical wireless communications (UWOC) [17–19]. In addition, it can also utilize white-light illumination systems as transmitters [20], providing safe and efficient communication solutions for enclosed environments such as underground mines, caves, and ship compartments.

In the past decade, InGaN blue laser diode (LD)-based high-speed VLC systems have attracted significant research interest [21–23], because they have a modulation bandwidth with several gigahertz (GHz) larger than other light sources such as light emitting diodes (LEDs) and superluminescent diodes (SLDs) [24]. In 2013, Watson et al. achieved a 1.4 GHz bandwidth with a 422-nm blue-violet LD and demonstrated a data rate of 2.5 Gbps [25]. Then,

* Corresponding author (email: chaoshen@fudan.edu.cn)

Table 1 Summary of the progress in high-speed blue InGaN LDs for VLC. The best results of bandwidth and data rate are in bold.

Year	λ (nm)	Threshold current (mA)	Slope efficiency (W/A)	Bandwidth (GHz)	Data rate (Gbps)	Modulation format	Ref.
2013	422	70	0.28	1.4 @ −3 dB	2.5	OOK	[25]
2015	450	34	1.2	1.5 @ −3 dB	9.0	64-QAM OFDM	[26]
2016	410	150	0.35	5.0 @ −3 dB	6.0	OOK	[27]
2017	450	35	0.89	3.0 @ −6 dB	18.0	16-QAM OFDM	[29]
2020	480	75	0.18	2.6 @ −10 dB	10.5	16-QAM OFDM	[32]
2022	450	20	0.61	3.4 @ −20 dB	14.6	DMT	[9]
2024	451	31	1.02	5.9 @ −3 dB	20.1	DMT	[35]
2025	448	30	0.73	5.4 @ −3 dB	21.8	DMT	[36]
This work	460	38	1.23	**8.4 @ −3 dB**	**20.0**	OOK	–
					33.0	PAM4	–
					37.1	DMT	–

Chi et al. achieved a data rate of 9 Gbps over a 5 m free space utilizing a commercial 1.5 GHz bandwidth InGaN blue LD combined with 64-quadrature amplitude modulation (QAM) orthogonal frequency division multiplexing (OFDM) [26]. Although higher-order modulation formats can effectively leverage the system's signal-to-noise ratio to enhance the data rate, increasing the bandwidth of LDs fundamentally expands the communication capacity of VLC systems. Subsequently, Lee et al. proposed using semipolar plane GaN to effectively suppress the quantum-confined Stark effect (QCSE), thus improving the recombination efficiency of the LD and achieving a −3 dB bandwidth of 5 GHz [27]. However, expensive substrates and the challenging epitaxial growth process remain significant barriers to implementing this approach [28].

Recently, research on high-speed VLC systems has been driven by advances in *c*-plane InGaN-based blue LDs. Some studies have used signal filters [29], external impedance matching [30], or distributed feedback gratings [31, 32] to improve the modulation performance of InGaN LDs, thus achieving high data rates, but these methods cannot significantly improve frequency response. Theoretically, the presence of strong polarization fields, high hole ionization energy, and low hole transport efficiency in the short-wavelength III-nitride materials system results in more carriers accumulating near the p-side quantum wells (QWs) [33, 34]. These will lead to saturation suppression in the differential gain for multiple quantum wells (MQWs) structures. Therefore, designing the resonant cavity, active region, and other epitaxial layers of InGaN LDs is crucial to achieving a large bandwidth. In 2024, we proposed the use of a 3 nm/5 nm double layer thin quantum well/barrier structure to enhance the differential gain of the LD. Furthermore, a short cavity length of 500 μm reduced the damping factor to 0.39 ns. The results demonstrated a blue LD with a modulation bandwidth of 5.9 GHz, achieving a data rate that exceeds 20 Gbps [35]. In 2025, Li et al. reported the impact of the thickness of the waveguide layer on the optical confinement factor and bandwidth of InGaN-based blue LDs. Using an optimized waveguide structure and a short cavity length, the blue LD achieved a −3 dB bandwidth of 5.4 GHz, allowing a data rate of 21.8 Gbps under discrete multitone (DMT) modulation [36]. These relevant research progresses on high-speed blue LDs for VLC systems are summarized in Table 1. Although significant improvements have been made in the communication capacity of InGaN-based blue LDs for VLC systems in recent years, achieving data rates beyond 30 Gbps with a simple modulation scheme to meet the demands of high-speed and low-cost links remains challenging. This highlights the urgent need for InGaN blue LDs with larger bandwidths.

In this work, we demonstrate a novel InGaN mini-LD structure, showing a large modulation bandwidth for high-speed VLC applications. We employ triple $In_{0.18}Ga_{0.82}N/In_{0.05}Ga_{0.95}N$ QWs and the 50 nm waveguide layer to enhance the carrier transport rate and uniform distribution in the active region. And the cavity length of the LD is reduced to 300 μm, effectively suppressing the damping factor of the dynamic response. Experimental results validate our design, with the resulting mini-LD achieving a −3 dB bandwidth of 8.4 GHz and a low damping factor of 0.21 ns. The device demonstrates groundbreaking communication performance under simple on-off keying (OOK) and four-level pulse amplitude modulation (PAM4), achieving data rates of 20 and 33 Gbps under the 7% hard-decision forward error correction (HD-FEC) threshold, respectively. These demonstrate that the blue mini-LD exhibits significant application potential in low-cost interconnect solutions. Furthermore, utilizing DMT modulation combined with bit-power loading technology, this mini-LD achieves a data rate exceeding 37 Gbps under the Shannon limit. To the best of our knowledge, this is the highest data rate ever achieved in a VLC system using a blue InGaN LD.

The remainder of this paper is organized as follows. Section 2 introduces the theoretical model used in the simulation and design of the high-speed blue InGaN mini-LD. Section 3 presents the fabrication processing of the

mini-LD. Section 4 then presents experimental results and discussions, including the emission, dynamic modulation, and communication performance of the mini-LD. Finally, the conclusion and future work are drawn in Section 5.

2 Simulation and design principle

To evaluate the modulation performance of MQWs InGaN LDs, the dynamic response model based on the self-consistent $k \cdot p$ method [37] and the 3D carrier drift-diffusion equations [38] has been established. The polarization properties of the wurtzite materials are also incorporated into the model. Spontaneous polarization in ternary nitride alloys is simulated using a linear interpolation between binary compounds with an added nonlinear term, while piezoelectric polarization is represented using a strain-dominated Vegard interpolation of the piezoelectric properties of binary constituents [39]. The interband gain broadening is implemented using the Landsberg scattering model [40]. These models are calculated using PICS3D (Version 2023) and Nuwa TCAD (Version 2023).

In our simulation, the high-speed blue LD has a 2 μm-wide ridge waveguide. The 3 μm Si-doped *c*-plane GaN contact layer has a density of 2×10^{18} cm^{-3}. The 0.3 μm upper cladding layer and 1 μm lower cladding layer are $Al_{0.07}Ga_{0.93}N$ with doping densities of 3×10^{18} cm^{-3} ([Si]) and 5×10^{18} cm^{-3} ([Mg]), respectively. The upper and lower waveguide layers both utilize $In_{0.03}Ga_{0.97}N$ and the n-type doping density is 2×10^{18} cm^{-3} ([Si]). The upper waveguide layer and the $In_{0.18}Ga_{0.82}N/In_{0.05}Ga_{0.95}N$ MQWs are not doped. An electron blocking layer (EBL) is 8 nm $Al_{0.18}Ga_{0.82}N$ with p-type doping ([Mg] = 5×10^{18} cm^{-3}). The p-contact layer is 100 nm GaN ([Mg] = 1×10^{19} cm^{-3}). Ohmic contacts are formed for both p-type and n-type electrodes. The polarization charge screening coefficient is 0.4 [41] and the spontaneous emission coupling coefficient is 1×10^{-4} [42]. The Shockley-Read-Hall lifetime is 30 ns [43] and the Auger recombination coefficient is 1×10^{-31} [22]. The reflectivities of the two facets are 0.99 and 0.4, respectively.

In order to evaluate the dynamic response performance of LD, the normalized transfer function $H(\omega)$ under small signal modulation is calculated based on [42, 44]:

$$H(\omega) = \frac{1}{1 + \mathrm{j}\omega\tau_s} \cdot \frac{\omega_R^2}{\omega_R^2 - \omega^2 + \mathrm{j}\gamma\omega}, \tag{1}$$

$$f_R = \frac{\omega_R}{2\pi} = \frac{1}{2\pi}\sqrt{\frac{\Gamma v_g}{qV}\frac{\partial g}{\partial N_c}\eta_i(I - I_{th})}, \tag{2}$$

$$\gamma = K f_R^2 + \gamma_0, \tag{3}$$

$$K = 4\pi^2\left(\tau_p + \frac{\varepsilon}{v_g\left(\partial g/\partial N_c\right)}\right). \tag{4}$$

Here, the frequency response $H(\omega)$ is divided into two parts. The first part, $1/(1+\mathrm{j}\omega\tau_s)$, represents the response of the carrier transport effect, where τ_s denotes the carrier ambipolar transport time. It represents the transmission time of electrons and holes through the waveguide layer. During modulation, if the carrier transport speed is too slow, charge accumulation occurs, forming parasitic capacitance around the active region. This parasitic response results in low-frequency roll-off in the frequency response. The second part of $H(\omega)$ corresponds to the intrinsic frequency response of the active region. The resonance frequency f_R of the LD is positively correlated with the differential gain $\partial g/\partial N_c$ (N_c is the carrier density) and the driving current level $I - I_{th}$. The damping γ suppresses the -3 dB bandwidth at high f_R, and is proportional to the square of f_R with a factor of K. The damping factor K is related to the photon lifetime τ_p, differential gain $\partial g/\partial N_c$, group velocity v_g and gain suppression factor ε (1×10^{-17} cm^3) caused by nonlinear effects. Therefore, the differential gain should be increased, while the damping factor and carrier ambipolar transport time should be decreased to achieve a high bandwidth in the InGaN-based mini-LD design.

Figure 1 shows the simulation results for designing the active region, waveguide layer, and resonant cavity, while also illustrating the regulation mechanisms of carrier transport and damping effects on the frequency response. Figure 1(a) shows the intrinsic frequency response curves for different mirror loss α_m under the same laser parameters. Obviously, increasing α_m can enhance the -3 dB bandwidth, as it reduces the τ_p, thus lowering the K factor. It is consistent with the description in (4). Since $\alpha_m = \ln(1/R_1R_2)/2L$ is related to the cavity length L (R_1 and R_2 are reflectivities of two facets), the damping effect can be controlled by reducing L, as shown in Figure 1(b). Notably, when L exceeds 100 μm, the reduction in τ_p dominates, leading to a decrease in K as L decreases. However, when L is reduced below 100 μm, the carrier density increases significantly, causing a dominant reduction in differential gain, which results in an observed increase in the value K. Meanwhile, the microcavity cleavage is limited to 300 μm

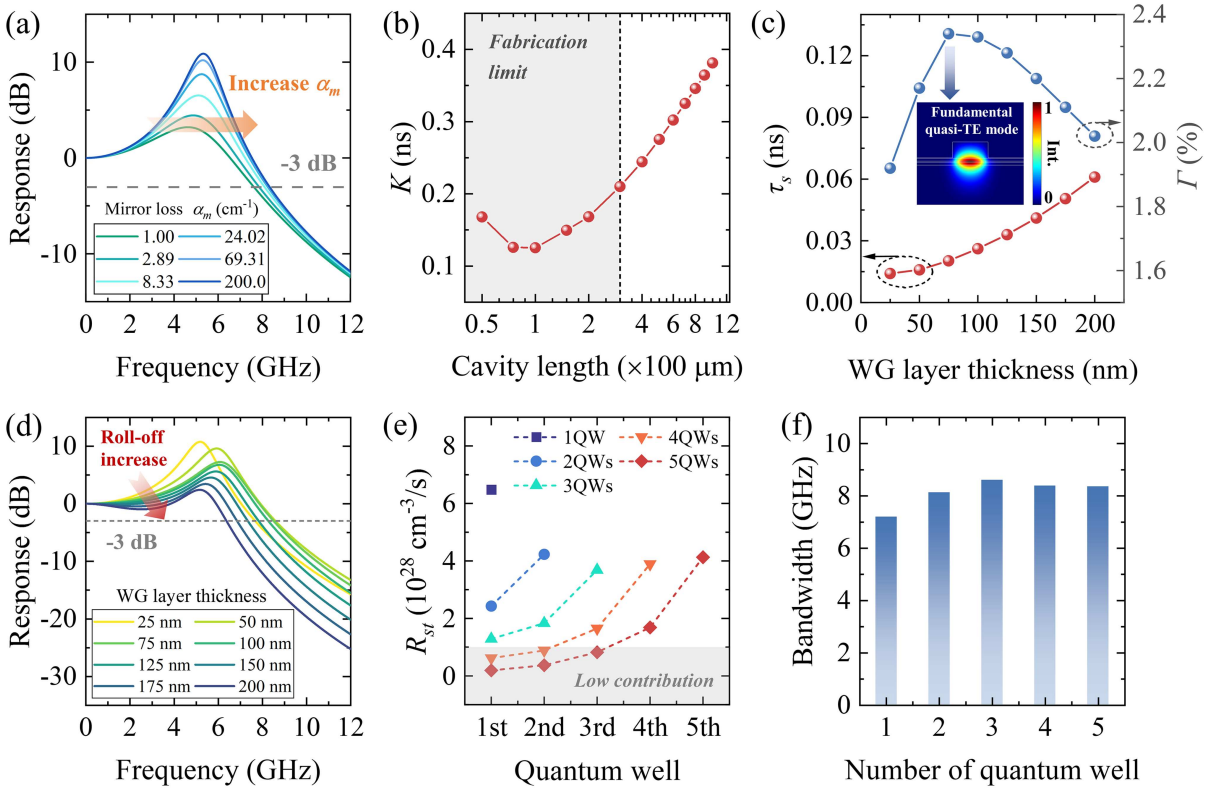

Figure 1 (Color online) Simulation of InGaN-based mini-LD. (a) Intrinsic frequency responses at different mirror loss α_m; (b) calculated damping factor K versus cavity length; (c) the extracted ambipolar transport time τ_s and optical confinement factor Γ under different waveguide (WG) layer thicknesses (the inset represents the fundamental quasi-TE mode of the 75 nm waveguide LD ('Int.' means intensity)); (d) frequency responses with carrier transport effect under various WG layer thicknesses of LD; (e) calculated recombination rates R_{st} for single to quintuple QWs (1–5 QWs) LD above threshold; (f) bandwidth versus number of quantum wells at $4I_{th}$ for 300 μm mini-LDs.

due to the strong stress in the GaN crystal. Therefore, a cavity length of 300 μm is chosen to significantly reduce the damping effect.

Figure 1(c) illustrates the impact of the thickness of the waveguide layer on the carrier ambipolar transport time τ_s and the optical confinement factor Γ. The carrier transport time τ_s almost quadruples with the waveguide thickness increasing from 25 to 200 nm, which significantly impacts the frequency response. As shown in Figure 1(d), LDs with thicker waveguide layers exhibit significant low-frequency roll-off in their frequency response, leading to a degradation in the −3 dB bandwidth. However, as the thickness of the waveguide layer increases, the optical confinement factor Γ initially increases, but subsequently decreases due to the optical field dispersion. This trend aligns with the variation in resonance frequency f_R observed in Figure 1(d). The inset shows the simulated fundamental quasi-TE mode of the LD with a 75 nm waveguide layer. In general, LD with a 50 nm waveguide layer exhibits the highest −3 dB bandwidth while maintaining a low τ_s.

Figure 1(e) presents the calculated stimulated recombination rate R_{st} for LD with a single QW to quintuple QWs. Due to the high ionization energy and low transport efficiency of the holes, more carriers tend to accumulate in the QWs closer to the p-side, resulting in most of the stimulated recombination occurring in these wells. For a single QW LD, the peak R_{st} is 6.48×10^{28} cm^{-3}/s. In the MQW structure, $R_{st} = v_g g N_p$ is mainly influenced by the carrier-dependent gain g and photon density N_p, which exhibits a decreasing trend from the p-side to the n-side. This imbalance leads to the saturation effect, suppressing the enhancement of differential gain in MQWs LD. As shown in Figure 1(f), this effect is reflected in the decrease in bandwidth for 3–5 QWs LD. The results indicate that the optimal number of QWs is three, which achieves the highest −3 dB bandwidth.

3 Fabrication of high-speed blue InGaN LD

Based on the simulation results, we fabricate blue InGaN mini-LDs with 300 μm cavity length. The device is grown on a *c*-plane GaN substrate using metal-organic chemical vapor deposition (MOCVD). Figure 2(a) shows the 3-D and cross-sectional epitaxial structure of the high-speed mini-LD. The epitaxial layers are designed to match the

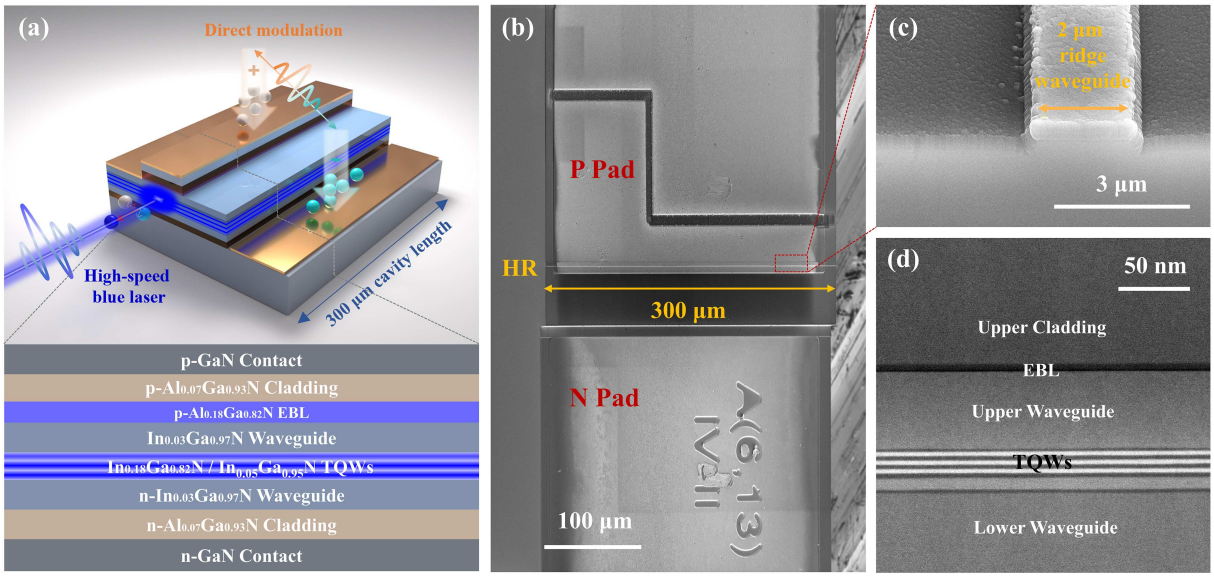

Figure 2 (Color online) Experimental details of high-speed blue InGaN mini-LD. (a) 3D model and epitaxial structure of the high-speed blue GaN LD; (b) scanning electron microscope (SEM) top-view image of the device; (c) bird-view SEM image; (d) STEM image of the device.

simulation, using a 3 nm/5 nm $In_{0.18}Ga_{0.82}N/In_{0.05}Ga_{0.95}N$ triple-QWs as the active region, and a 50 nm waveguide layer is implemented to alleviate the carrier transport effect. The n-$In_{0.03}Ga_{0.97}N$ waveguide has a doping density of 2×10^{18} cm^{-3} ([Si]). The 8 nm $Al_{0.18}Ga_{0.82}N$ with p-type doping ([Mg] $= 5 \times 10^{18}$ cm^{-3}) is used as the EBL layer. The 0.3 μm (p-type) and 1 μm (n-type) cladding layer is $Al_{0.07}Ga_{0.93}N$ with doping densities of 3×10^{18} cm^{-3} ([Si]) and 5×10^{18} cm^{-3} ([Mg]), respectively. The Mg-doped p-contact layer is 100 nm GaN ([Mg] $= 1 \times 10^{19}$ cm^{-3}).

The top-view scanning electron microscope (SEM) images of the device are shown in Figure 2(b). UV photolithography and inductively coupled plasma (ICP) etching are used to pattern the epitaxial layers into a 2 μm narrow ridge waveguide. The 200 nm SiO_2 is sputtered onto the chip for passivation and electrical isolation. The Pd/Ti/Pt/Ti/Au and Ti/Pt/Ti/Au metal stacks are deposited as p-type and n-type electrodes, respectively. Here, focused ion beam (FIB) etching is employed to define a small p-electrode area. This approach effectively reduces the parasitic capacitance associated with the p-electrode while retaining the surrounding metal to facilitate efficient heat dissipation. A 300 μm resonant cavity is formed by mechanical cleaving. The front and rear facets are coated with pairs of SiO_2/TiO_2, with a high reflectivity (HR) of 0.99 and a low reflectivity of 0.4, respectively. Figure 2(c) clearly shows the front facet and the 2 μm ridge waveguide, which indicates the cleaved cavity facet exhibits high verticality. The scanning transmission electron microscope (STEM) image of the epitaxial layers is presented in Figure 2(d). The image clearly shows the triple QWs (TQWs), the upper and lower waveguide layers, the EBL layer, and the upper cladding layer, all of which demonstrate high crystalline quality. These results indicate that the structural parameters of the fabricated device closely match our simulation design.

4 Experimental results and discussions

Figure 3(a) demonstrates the light-current-voltage (L-I-V) characteristics of the fabricated high-speed blue mini-LD. The mini-LD is tested under continuous-wave (CW) operation using a Keithley 2520 source meter, with pulse mode employed to eliminate the self-heating effect. The inset illustrates the lasing state of the mini-LD. The result shows that the device has a turn-on voltage of 3.2 V, a threshold current of 38 mA, and a high slope efficiency η_{se} of 1.23 W/A. And the linear L-I curve indicates the absence of significant mode-hopping or efficiency droop. Then, the quantum efficiency η_i can be calculated as

$$\eta_i = \frac{\alpha_i + \alpha_m}{F \cdot \alpha_m} \cdot \frac{q\,\eta_{se}}{h\nu}. \tag{5}$$

Here, the internal cavity loss α_i is estimated to be 10 cm^{-1}, and the factor $F \approx 1$ is the fraction of power not reflected into the cavity that escapes as a useful output from the output coupling mirror. Therefore, the quantum efficiency η_i is 71%. Compared to our previous work [35], the enhancement of carrier transport in the active region can improve the quantum and slope efficiency, which will provide a sufficient signal-to-noise ratio (SNR) to

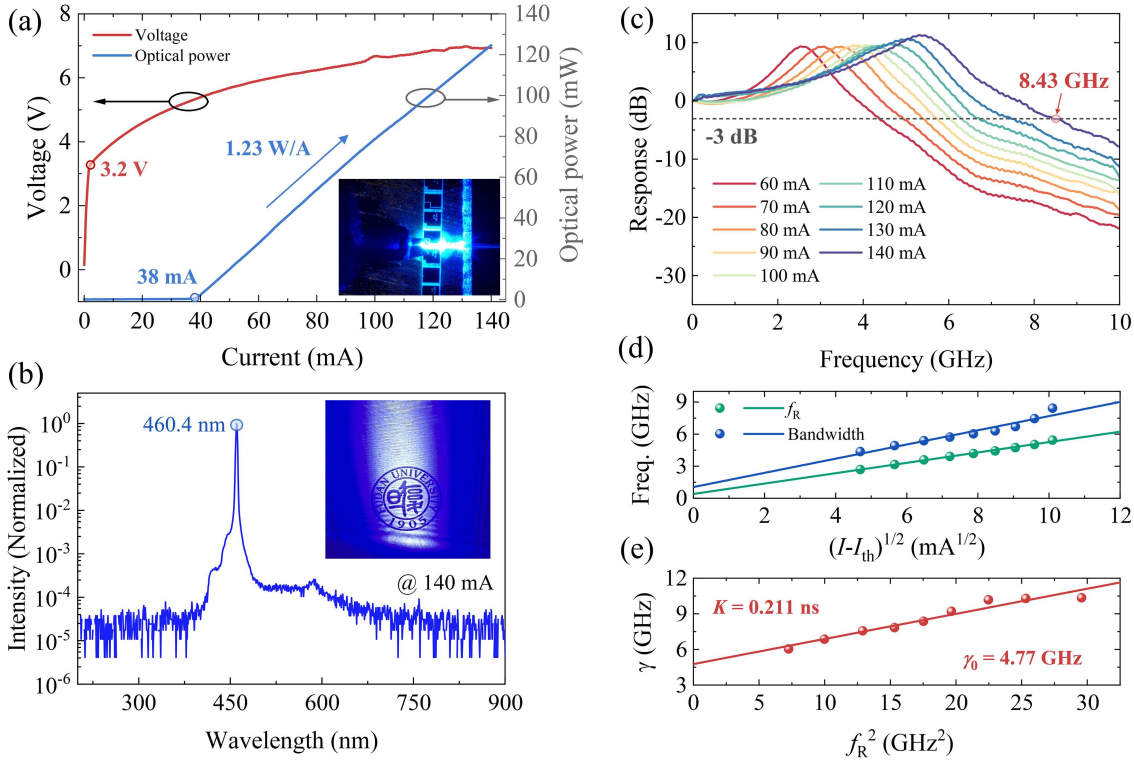

Figure 3 (Color online) Emission and dynamic modulation performance of the blue mini-LD. (a) Light-current-voltage (L-I-V) of the blue mini-LD (the inset illustrates the lasing of the mini-LD); (b) electroluminescence spectrum at 140 mA (the inset shows the far-field pattern of emission from the mini-LD); (c) measured frequency response curves of the blue mini-LD under various driven currents; (d) resonance frequency f_R and bandwidth versus $(I - I_{th})^{1/2}$; (e) damping parameter γ versus the square of the f_R.

support high-order modulation [45]. The electroluminescence (EL) spectrum is measured using a high-sensitivity spectrometer (Ocean QE Pro). Figure 3(b) shows the normalized EL spectrum at 140 mA. The peak wavelength is 460.4 nm, and the inset shows the far-field emission pattern.

Subsequently, the dynamic modulation characteristics of the blue LD are experimentally investigated. In the measurement, a network analyzer (Agilent N5230C PNA-L) is used to characterize the S21 parameter of the two-port network. A high-speed photodetector (PD, Newport 818-BB-45A) is used as the receiver. After calibration, removal of the free-running response and normalization, the intrinsic frequency response of the device is obtained, as shown in Figure 3(c). The resonance peak in the frequency response curve originates from carrier-photon resonance. The resonance frequency increases significantly with the driving current, leading to an enhancement of the −3 dB bandwidth, which is consistent with the description in (1) and (2). At 140 mA, a high −3 dB bandwidth of 8.43 GHz is achieved. However, further increasing the current leads to a noticeable self-oscillation effect [46], resulting in response instability and increased noise. Therefore, frequency responses beyond 140 mA are not shown here. The extracted resonance frequency f_R and −3 dB bandwidth are plotted against the current level $(I - I_{th})^{1/2}$ in Figure 3(d). The fitted frequency response efficiency $df_R/d(I - I_{th})^{1/2}$ is 0.49 GHz/mA$^{1/2}$. And the bandwidth efficiency is 0.66 GHz/mA$^{1/2}$. Such a high direct modulation efficiency enables the mini-LD to achieve a large bandwidth under high driven current. The result also indicates that f_R is almost proportional to $(I - I_{th})^{1/2}$, suggesting that the gain suppression caused by nonlinear optical phenomena is almost negligible at bias currents up to 140 mA. Additionally, Figure 3(e) demonstrates the damping effect of the device and illustrates the relationship between γ and the square of f_R. By fitting these data points to (3), the damping factor K is determined to be 0.211 ns, with an offset γ_0 of 4.77 GHz. The K factor of this mini-LD is lower than that of other reported InGaN LDs [21, 29], demonstrating its superior dynamic modulation performance.

Then, we construct a real experimental setup of the VLC system to demonstrate the communication capabilities of the mini-LD. Figure 4 shows the BER performance of the system and the eye diagrams for the OOK and PAM4 modulation formats. The details of the experimental setup and de/modulation principles are demonstrated in the supporting information. As shown in Figure 4(a), BER increases with the baud rate for both modulation schemes. This trend is attributed to the constant power constraint in intensity modulation and direct detection (IM/DD) systems, where an increase in signal bandwidth results in a reduced average SNR, leading to higher BER. The

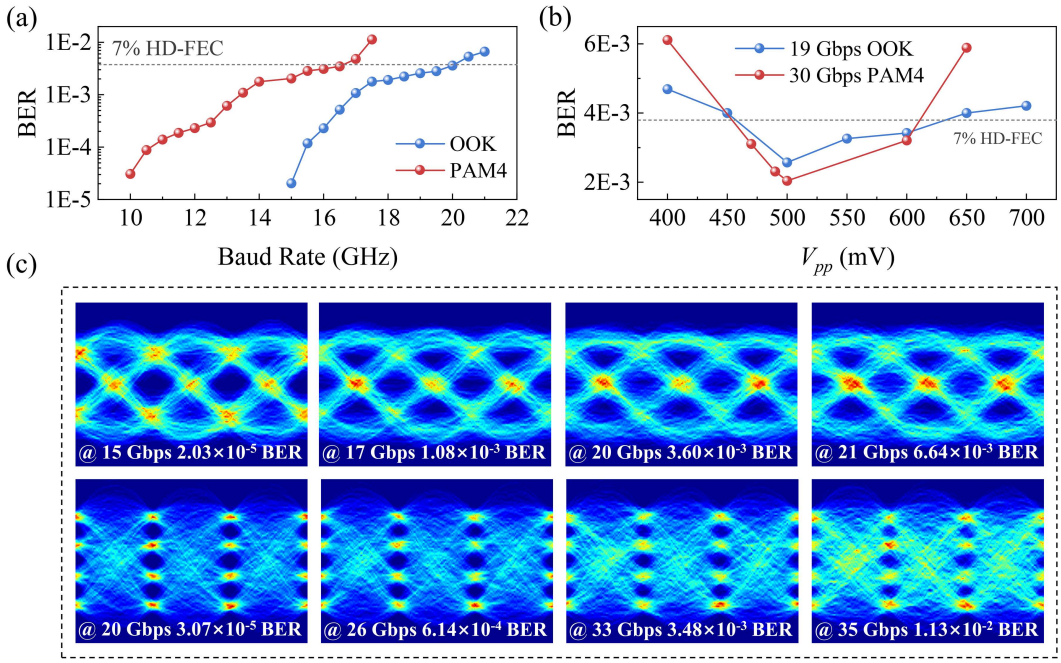

Figure 4 (Color online) Communication performance of the blue LD with OOK/PAM4 modulation. (a) BER for PAM4 and OOK modulation formats at various baud rates; (b) BER of OOK (19 Gbps) and PAM4 (30 Gbps) systems at a fixed data rate versus the modulation signal peak-to-peak voltage (V_{pp}); (c) eye diagrams of OOK and PAM4 systems at various data rates.

7% HD-FEC threshold (3.8×10^{-3}) is marked as a gray dashed line for reference, indicating the maximum BER tolerance for forward error correction. Due to the frequency response limitations of high-speed PD, significant noise appears in the spectrum beyond 8 GHz. This prevents the system from maintaining the SNR required for PAM4 modulation beyond a baud rate of 16.5 GHz, leading to a sharp increase in BER beyond the FEC threshold. In contrast, OOK modulation requires a lower SNR, and its BER only exceeds the threshold beyond a baud rate of 10 GHz. These results demonstrate that the highest achievable data rates before reaching the FEC threshold are 20 Gbps for OOK and 33 Gbps for PAM4. Furthermore, the dependence of BER on the peak-to-peak voltage (V_{pp}) of the OOK and PAM4 signals is demonstrated in Figure 4(b). For 19 Gbps OOK and 30 Gbps PAM4 modulation, the BER initially decreases with increasing V_{pp} due to the improved system SNR. However, as V_{pp} continues to increase, power saturation and nonlinear modulation effects introduce additional noise, leading to an increased BER. The results indicate that 19 Gbps OOK and 30 Gbps PAM4 modulation maintain dynamic operating ranges of 174 and 157 mV below the FEC threshold, respectively. The optimal operating V_{pp} for these modulation formats is found to be 500 mV, achieving BERs of 2.57×10^{-3} and 2.04×10^{-3}, respectively. Figure 4(c) presents the eye diagrams of OOK and PAM4 at different data rates. At lower data rates, such as OOK below 17 Gbps and PAM4 below 26 Gbps, the eye openings remain clear, indicating good signal integrity and low BERs. As the data rate increases, inter-symbol interference (ISI) and noise progressively degrade the eye diagrams, reducing the eye opening and leading to an increase in BERs. The eye diagram of 35 Gbps PAM4 signal shows an average amplitude ISI of 14.7% UI and a root mean square (RMS) timing jitter of 13.01 ps, indicating poor signal integrity. The calculated BER reaches 1.13×10^{-2}. Therefore, before the 7% HD-FEC threshold, the blue mini-LD-based VLC system can achieve a data rate of 33 Gbps by using PAM4 modulation.

To further explore the maximum communication capacity of this high-speed blue mini-LD-based VLC system under the Shannon limit, DMT modulation combined with a Levin-Campello (LC) bit-power loading algorithm is employed [9]. This algorithm optimizes bits and power allocation with minimum power redundancy. Figure 5(a) illustrates the variation of data rate with DMT modulation signal bandwidth. All BERs are below the FEC threshold. As the signal bandwidth increases from 6 to 7.5 GHz, the data rate continues to rise since the reduction in average SNR is slower than the increase in bandwidth, resulting in a net gain in the transmission capacity. However, as the bandwidth exceeds 7.5 GHz, the data rate starts to decline. This is because the decrease in average SNR surpasses the bandwidth expansion, leading to the saturation of the trade-off between spectral efficiency (SE) and the signal bandwidth. Moreover, the overall frequency response of the system link, including cables, exhibits more than 5 dB attenuation in high frequency range, while the photodetector (PD) introduces significant noise in this region. These factors cause a drop in SNR beyond 8 GHz, limiting effective bit loading and power allocation. The

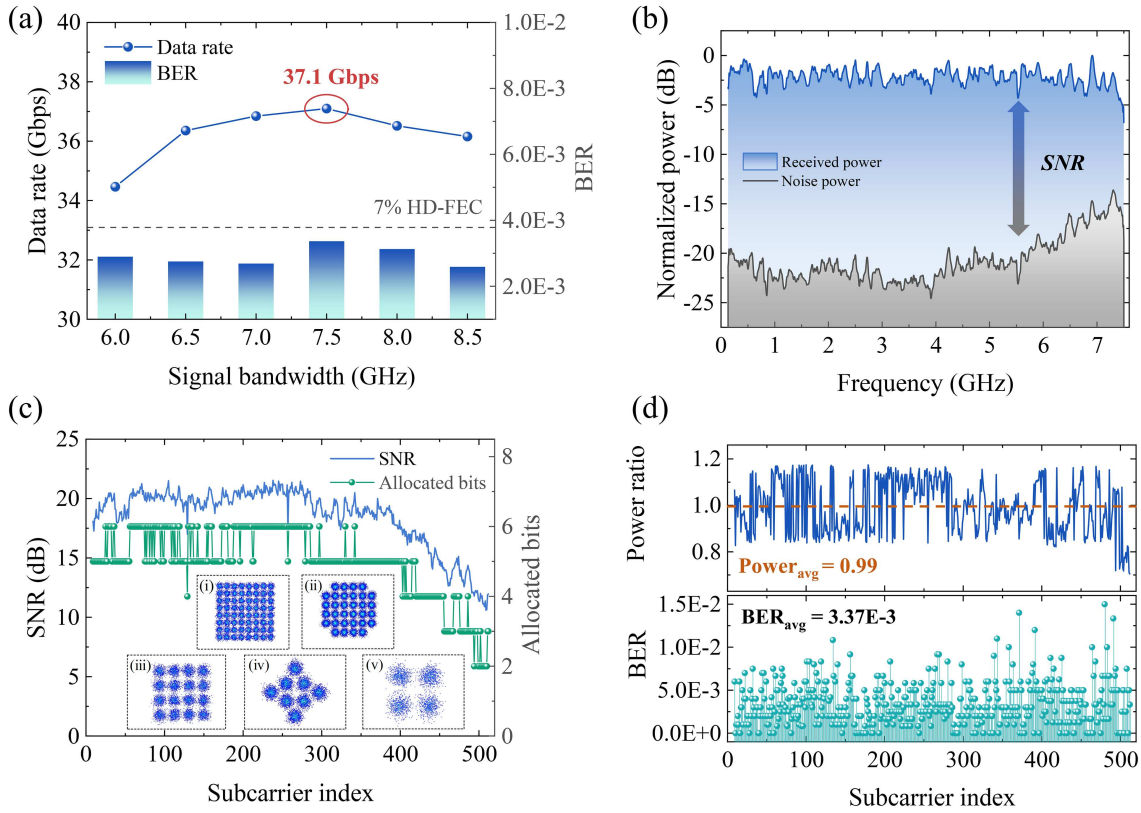

Figure 5 (Color online) Communication performance of the blue mini-LD-based VLC link. (a) Data rate and BER versus signal bandwidth of DMT modulation; (b) received signal and noise power spectra at a 7.5 GHz signal bandwidth; (c) bit allocation and estimated SNR at a 7.5 GHz signal bandwidth using the LC algorithm; (d) power ratio and BER of each subcarrier at 37.1 Gbps.

results indicate that the optimal DMT signal bandwidth is 7.5 GHz, achieving a maximum data rate of 37.1 Gbps. Figure 5(b) presents the received signal and noise power spectra at a 7.5 GHz bandwidth, with their difference representing the SNR spectrum of the VLC link. The calculated average SNR is 18.55 dB. It can be observed that at 7.5 GHz, the noise power increases by 5 dB compared to the low-frequency region. This rise is attributed to the frequency response limitations of various system components, including cables, adapters, and the PD. Figure 5(c) illustrates the bit allocation and measured SNR spectrum for the QAM-DMT signal at the maximum data rate of 37.1 Gbps. Using the LC algorithm, the VLC system based on the blue LD achieves a high SE of 5.03 bits/s/Hz at the optimal modulation bandwidth of 7.5 GHz. The allocated bit distribution closely follows the SNR variations, with a maximum allocation of 6 bits per subcarrier, enabling support for 64-QAM modulation. However, due to SNR degradation at higher frequencies, the minimum modulation level is limited to 4-QAM. The inset presents the received constellation diagrams for different modulation formats, including 64-QAM, 32-QAM, 16-QAM, 8-QAM, and 4-QAM. Figure 5(d) shows the normalized power allocation for each subcarrier and the calculated BER at a data rate of 37.1 Gbps for the DMT signal. The initial normalized power allocation is set to 1.0. According to the LC algorithm, in each iteration, subcarriers with power redundancy contribute their excess power to those requiring the minimum additional power to increase their bit loading by 1 bit. After multiple iterations, the final power distribution is determined by the measured SNR and the initial bit allocation. At the highest data rate, the normalized power ratio of the DMT signal fluctuates between 0.7 and 1.2 with an average of 0.99, reflecting the efficient power loading strategy to maximize the SE while maintaining BER performance. The calculated average BER is 3.37×10^{-3}, which remains below the 7% HD-FEC threshold, confirming the system's reliability at this high data rate. These results highlight the excellent communication performance of our designed mini-LD.

5 Conclusion

This work designs and fabricates a large-bandwidth blue InGaN mini-LD and demonstrates its potential for VLC applications. A theoretical model and numerical analysis are established to optimize the active region, waveguide layer, and cavity structure. By employing a triple 3 nm/5 nm $In_{0.18}Ga_{0.82}N/In_{0.05}Ga_{0.95}N$ QWs, the increased

differential gain of the LD can enhance the relaxation oscillation frequency and bandwidth. The 50 nm waveguide layer is used to shorten the carrier ambipolar transport time. Meanwhile, reducing the cavity length to 300 μm can effectively suppress the damping effect, thus improving the −3 dB bandwidth. The fabricated blue InGaN LD achieves a high slope efficiency of 1.23 W/A, with a high −3 dB bandwidth of 8.4 GHz at 140 mA and a low damping factor of 0.211 ns. When applied in a VLC system, it allows data rates of 20.0, 33.0, and 37.1 Gbps under OOK, PAM4, and DMT modulation, respectively. To the best of our knowledge, these results represent the highest −3 dB bandwidth and data rate for a blue InGaN LD.

In future work, the method of this work can be extended to a fully coupled thermal-electrical-optical model by experimental calibration, combined with various channel models [47–49], which will reveal the thermal performance of the LD, the system noise mechanisms, and the error analysis. In addition, intelligent heuristic optimization algorithms [50] or physics-informed neural networks [51] can also be introduced to accelerate the device design process. Such advancements are essential to meet the stringent thermal stability requirements of optical interconnects in GPU/XPU computing environments [52]. Also, leveraging this high-speed laser chip in combination with short-wavelength photon-photon resonance techniques could significantly enhance the modulation bandwidth when integrated into advanced visible-light passive external cavity platforms such as Si_3N_4 waveguide [53, 54]. These will facilitate the development of high-speed InGaN-based blue LDs and cost-effective visible light photonic integration technologies, providing critical device-level support for next-generation 6G-oriented optical networks.

Acknowledgements This work was partially supported by National Natural Science Foundation of China (Grant Nos. 624B2045, 62274042), Key Research and Development Program of Jiangsu Province (Grant No. BE2021008-5), and Shanghai Rising-Star Program (Grant No. 24QB2705400).

Supporting information Appendixes A and B. The supporting information is available online at info.scichina.com and link.springer.com. The supporting materials are published as submitted, without typesetting or editing. The responsibility for scientific accuracy and content remains entirely with the authors.

References

1 Kadir E A, Shubair R, Rahim S K A, et al. B5G and 6G: next generation wireless communications technologies, demand and challenges. In: Proceedings of International Congress of Advanced Technology and Engineering (ICOTEN), 2021. 1–6
2 Salahdine F, Han T, Zhang N. 5G, 6G, and beyond: recent advances and future challenges. Ann Telecommun, 2023, 78: 525–549
3 You X H, Huang Y M, Zhang C, et al. When AI meets sustainable 6G. Sci China Inf Sci, 2025, 68: 110301
4 Cui Q M, You X H, Wei N, et al. Overview of AI and communication for 6G network: fundamentals, challenges, and future research opportunities. Sci China Inf Sci, 2025, 68: 171301
5 Wang C-X, Lv Z, Huang C, et al. An enhanced 6G pervasive channel model towards standardization. Sci China Inf Sci, 2025, 68: 162301
6 Matheus L E M, Vieira A B, Vieira L F M, et al. Visible light communication: concepts, applications and challenges. IEEE Commun Surv Tutorials, 2019, 21: 3204–3237
7 Chi N, Zhou Y, Wei Y, et al. Visible light communication in 6G: advances, challenges, and prospects. IEEE Veh Technol Mag, 2020, 15: 93–102
8 Chi N, Haas H, Kavehrad M, et al. Visible light communications: demand factors, benefits and opportunities [Guest Editorial]. IEEE Wireless Commun, 2015, 22: 5–7
9 Hu J, Hu F, Jia J, et al. 46.4 Gbps visible light communication system utilizing a compact tricolor laser transmitter. Opt Express, 2022, 30: 4365–4373
10 Luo Z, Lin X, Lu Z, et al. 113 Gbps rainbow visible light laser communication system based on 10λ laser WDM emitting module in fiber-free space-fiber link. Opt Express, 2024, 32: 2561–2573
11 Shi J, Fang X, Niu W, et al. 800 Gbps visible light communication system employing WDM and OAM multiplexing. In: Proceedings of the 20th International Conference on Optical Communications and Networks (ICOCN), 2022. 1–3
12 Ndjiongue A R, Ngatched T M N, Dobre O A, et al. VLC-based networking: feasibility and challenges. IEEE Netw, 2020, 34: 158–165
13 Qi Z Q, Xie M Y, Wang L N, et al. Full-duplex ultraviolet light communication network for space-chip interconnection. Sci China Inf Sci, 2025, 68: 209301
14 Yin L, Haas H. Physical-layer security in multiuser visible light communication networks. IEEE J Sel Areas Commun, 2017, 36: 162–174
15 Ong Z, Rachim V P, Chung W Y. Novel electromagnetic-interference-free indoor environment monitoring system by mobile camera-image-sensor-based VLC. IEEE Photonics J, 2017, 9: 1–11
16 Dong C, Fu Q, Wang K, et al. The model and characteristics of polarized light transmission applicable to polydispersity particle underwater environment. Optics Lasers Eng, 2024, 182: 108449
17 Hu J, Guo Z, Shi J, et al. A metasurface-based full-color circular auto-focusing airy beam transmitter for stable high-speed underwater wireless optical communications. Nat Commun, 2024, 15: 2944
18 Guo C, Li Z, Zha L, et al. Diffuse-LOS optical wireless communication across wavy water-air-interface using UVA light. IEEE Access, 2024, 12: 107959
19 Qi Z Q, Wang L M, Liang Y Z, et al. Mobile wireless light communication network. Sci China Inf Sci, 2025, 68: 174301
20 Hou Y, Wang Z, Liu M, et al. Wide field-of-view laser-based white light transmitter for visible light communications. Opt Lett, 2024, 49: 2805–2808
21 Sun Y, Zhou K, Sun Q, et al. Room-temperature continuous-wave electrically injected InGaN-based laser directly grown on Si. Nat Photon, 2016, 10: 595–599
22 Zhong Z, Lu S, Li J, et al. Design and fabrication of high power InGaN blue laser diode over 8 W. Optics Laser Tech, 2021, 139: 106985
23 Trageser E, Zhang H, Palmer S, et al. Blue GaN-based DFB laser diode with sub-MHz linewidth. Opt Express, 2024, 32: 23372–23380
24 Guo Y, Alkhazragi O, Kang C H, et al. A tutorial on laser-based lighting and visible light communications: device and technology. Chin Opt Lett, 2019, 17: 040601
25 Watson S, Tan M, Najda S P, et al. Visible light communications using a directly modulated 422 nm GaN laser diode. Opt Lett, 2013, 38: 3792–3794
26 Chi Y C, Hsieh D H, Tsai C T, et al. 450-nm GaN laser diode enables high-speed visible light communication with 9-Gbps QAM-OFDM. Opt Express, 2015, 23: 13051–13059
27 Lee C, Zhang C, Becerra D L, et al. Dynamic characteristics of 410 nm semipolar ($20\overline{2}1$) III-nitride laser diodes with a modulation bandwidth of over 5 GHz. Appl Phys Lett, 2016, 109: 101104

28 Wang T. Topical review: development of overgrown semi-polar GaN for high efficiency green/yellow emission. Semicond Sci Technol, 2016, 31: 093003
29 Huang Y F, Chi Y C, Kao H Y, et al. Blue laser diode based free-space optical data transmission elevated to 18 Gbps over 16 m. Sci Rep, 2017, 7: 10478
30 Wang W C, Wang H Y, Lin G R. Ultrahigh-speed violet laser diode based free-space optical communication beyond 25 Gbit/s. Sci Rep, 2018, 8: 13142
31 Najda S P, Perlin P, Suski T, et al. GaN laser diode technology for visible-light communications. Electronics, 2022, 11: 1430
32 Holguin-Lerma J A, Kong M, Alkhazragi O, et al. 480-nm distributed-feedback InGaN laser diode for 10.5-Gbit/s visible-light communication. Opt Lett, 2020, 45: 742–745
33 Marcinkevičius S, Yapparov R, Kuritzky L Y, et al. Interwell carrier transport in InGaN/(In)GaN multiple quantum wells. Appl Phys Lett, 2019, 114: 151103
34 Hu J, Jia H, Gu Z, et al. Investigation on large modulation bandwidth InGaN-based blue laser diodes. Optics Laser Tech, 2025, 185: 112601
35 Wang J, Hu J, Guan C, et al. High-speed GaN-based laser diode with modulation bandwidth exceeding 5 GHz for 20 Gbps visible light communication. Photon Res, 2024, 12: 1186–1193
36 Li Z, Xu Z, Li S, et al. 21.79/17.49 Gbps full-duplex visible light communication enabled by short-cavity blue and green InGaN/GaN laser diodes. J Lightwave Technol, 2025, 43: 3348–3357
37 Chuang S L, Chang C S. $k \cdot p$ method for strained wurtzite semiconductors. Phys Rev B, 1996, 54: 2491–2504
38 Laux S E. Techniques for small-signal analysis of semiconductor devices. IEEE Trans Electron Dev, 2005, 32: 2028–2037
39 Fiorentini V, Bernardini F, Ambacher O. Evidence for nonlinear macroscopic polarization in III-V nitride alloy heterostructures. Appl Phys Lett, 2002, 80: 1204–1206
40 Landsberg P. Electron interaction effects on recombination spectra. Physica Status Solidi (B), 1966, 15: 623–626
41 Zhang Y, Qiu X, Chu C, et al. Impact of an AlGaN thin insertion layer in the p-GaN region on InGaN/GaN vertical-cavity surface-emitting laser diodes. Micro Nanostruct, 2022, 171: 207425
42 Coldren L A, Corzine S W, Mashanovitch M L. Diode Lasers and Photonic Integrated Circuits. Hoboken: John Wiley & Sons, 2012
43 Alahyarizadeh G, Aghajani H, Mahmodi H, et al. Analytical and visual modeling of InGaN/GaN single quantum well laser based on rate equations. Optics Laser Tech, 2012, 44: 12–20
44 Nagarajan R, Ishikawa M, Fukushima T, et al. High speed quantum-well lasers and carrier transport effects. IEEE J Quantum Electron, 1992, 28: 1990–2008
45 Hu F, Chen S, Zhang Y, et al. High-speed visible light communication systems based on Si-substrate LEDs with multiple superlattice interlayers. PhotoniX, 2021, 2: 16
46 Tager A A, Petermann K. High-frequency oscillations and self-mode locking in short external-cavity laser diodes. IEEE J Quantum Electron, 2002, 30: 1553–1561
47 Elsayed E E. Investigations on modified OOK and adaptive threshold for wavelength division multiplexing free-space optical systems impaired by interchannel crosstalk, atmospheric turbulence, and ASE noise. J Opt, 2024, doi: 10.1007/s12596-024-01929-4
48 Singh M, Elsayed E E, Alayedi M, et al. Performance analysis in spectral-amplitude-coding-optical-code-division-multiple-access using identity column shift matrix code in free space optical transmission systems. Opt Quant Electron, 2024, 56: 795
49 Elsayed E E, Yousif B B. Performance evaluation and enhancement of the modified OOK based IM/DD techniques for hybrid fiber/FSO communication over WDM-PON systems. Opt Quant Electron, 2020, 52: 385
50 Sun J, Zhou S, Lin Q. A high-precision and fast modeling method for amplifiers. Int J Numer Model, 2025, 38: e70051
51 Wright L G, Onodera T, Stein M M, et al. Deep physical neural networks trained with backpropagation. Nature, 2022, 601: 549–555
52 Rumley S, Bahadori M, Polster R, et al. Optical interconnects for extreme scale computing systems. Parallel Computing, 2017, 64: 65–80
53 Corato-Zanarella M, Gil-Molina A, Ji X, et al. Widely tunable and narrow-linewidth chip-scale lasers from near-ultraviolet to near-infrared wavelengths. Nat Photon, 2023, 17: 157–164
54 Shao S, Li J, Wu Y, et al. Modulation bandwidth enhanced self-injection locking laser with an external high-Q microring reflector. Opt Lett, 2021, 46: 3251–3254